The Astrophysical Journal, 967:127 (6pp), 2024 June 1 https://doi.org/10.3847/1538-4357/ad445e

Multiband Nonthermal Radiative Study of PeVatron Candidate Pulsar Wind Nebula HESS J1849-000

Bo-Tao Zhu[1,3], Fang-Wu Lu[2,3], and Li Zhang[3]
[1] College of Science, Yunnan Agricultural University, Kunming, 650201, People's Republic of China
[2] Department of Physics, Yuxi Normal University, Yuxi, 653100, People's Republic of China; sfweb@yxnu.edu.cn
[3] Department of Astronomy, Key Laboratory of Astroparticle Physics of Yunnan Province, Yunnan University, Kunming, 650091, People's Republic of China; lizhang@ynu.edu.cn
Received 2024 January 17; revised 2024 April 23; accepted 2024 April 25; published 2024 May 28

Abstract

Pulsar wind nebula HESS J1849-000 is one of the sources that may emit PeV γ-ray photons based on the recent measurement by the Tibet Air Shower Array and the Large High Altitude Air Shower Observatory. We use a time-dependent model to investigate the nonthermal radiative properties of HESS J1849-000. Observed multiband data are produced well by relativistic leptons through synchrotron radiation and inverse Compton processes, and the particle transport and cooling processes are analyzed. Our results show that the particle adiabatic loss dominates over the synchrotron loss and inverse Compton losses, and the particle advection dominates over diffusion for the low-energy band. On the other hand, the particle synchrotron loss dominates over the adiabatic loss and inverse Compton losses, and the diffusion dominates over advection for the high-energy band. Furthermore, particle transport would be playing a significant role in the low-energy band, whereas the particle cooling processes may play a more important role in the high-energy band. The current diffusion coefficient $3.4 \times 10^{26}\,\mathrm{cm^2\,s^{-1}}$ at an electron energy of 1 TeV is derived, which implies a slow diffusion mechanism may occur within the nebula. More importantly, our model suggests that the particle's maximum energy is 3.6 PeV, which makes HESS J1849-000 a PeVatron candidate.

Unified Astronomy Thesaurus concepts: Pulsars (1306); Pulsar wind nebulae (2215)

1. Introduction

As a neutron star rapidly rotates, it produces a highly relativistic particle (electron and positron) wind, which in turn interacts with the surrounding environment as it expands outward creating a pulsar wind nebula (PWN; Gaensler & Slane 2006). PWNe are the most powerful particle accelerators within our Galaxy, as evidenced by detections of very high energy photons emitted from them (H.E.S.S. Collaboration 2018a; Cao et al. 2021a, 2021b), plausibly from cosmic-ray interactions with energy close to or up to 1 PeV. Recently, Cao et al. (2024) presented the first catalog of very-high-energy and ultra-high-energy γ-ray sources detected by the Large High Altitude Air Shower Observatory (LHAASO). From the catalog, 35 sources are found with associated pulsars. Detecting these Galactic sources is the key to the origin of the highest-energy Galactic cosmic rays, as well as a better understanding of the particle acceleration, radiation, cooling, and transport mechanisms.

HESS J1849-000 is a TeV emission source detected in the HESS Galactic Plane survey (H.E.S.S. Collaboration 2018b), and it was found to be spatially coincident with the soft γ-ray source IGR J1849-000, which was first discovered by INTEGRAL (Molkov et al. 2004). XMM-Newton observations resolved the INTEGRAL source into a pulsar + PWN system (Terrier et al. 2008). Gotthelf et al. (2011) used the Rossi X-ray Timing Explorer (RXTE) observations to identify the energetic pulsar of HESS J1849-000 and PSR J1849-0001 exhibits a spin period of $P = 38.52$ ms, a period derivative of $\dot{P} = 14.14 \times 10^{-15}\,\mathrm{s\,s^{-1}}$, and current spin-down luminosity of $L(t_{\rm age}) = 9.77 \times 10^{36}\,\mathrm{erg\,s^{-1}}$ (Manchester et al. 2005; Gotthelf et al. 2011). HESS J1849-000 is also identified as an extended PWN around PSR J 1849-0001 by the latter researchers (Kuiper & Hermsen 2015; Vleeschower Calas et al. 2018).

To date, there is no known radio PWN coincident with HESS J1849-000 (Green 2014; Anderson et al. 2017; Green 2019). Very recently, Kim et al. (2024) used Chandra, XMM-Newton, NICER, Swift, and NuSTAR to measure both the X-ray spectrum and the radial profiles of the PWN's brightness and photon index, and then employed a spatially dependent emission scenario to explain the broadband data. In addition, Gagnon et al. (2023) also explored the PWN morphology on arcsecond and arcminute scales and measured the spectra of different regions of the PWN by analyzing the new and old Chandra data. HESS J1849-000 is not detected in the GeV band by the Fermi-LAT. Follow-up observation of H.E.S.S. analysis confirmed the existence of a source HESS J1849-000. The best-fit position is located less than $0.^{\circ}03$ from the PSR J 1849-0001 position, and the best-fit size of the TeV emission is $0.^{\circ}09$ (H.E.S.S. Collaboration 2018b). Recently, Amenomori et al. (2023) measured the spectrum of HESS J1849-000 at the TeV energy band and found no evidence of cut-off up to 740 TeV by the Tibet Air Shower Array (TASA), making the source a PeV candidate. Furthermore, LHAASO collaboration observation found also that the extended sources LHAASO J1848-0001 around PSR J 1849-0001, which can emit PeV γ-ray photons, and the best-fit size of the emission is less than $0.^{\circ}09$ (Cao et al. 2024). Because of this spatial coincidence, we considered that these are two separate detections of the same γ-ray extended source.

In this paper, we investigate the multiband nonthermal radiative properties of pulsar wind nebula HESS J1849-000

powered by the pulsar PSR J1849-0001 based on a time-dependent model. In Section 2, the detail of the model is described. The results of the nebula are presented in Section 3. Finally, our summary and discussion are presented in Section 4.

2. Model Description

The particle transport equation within nebulae can be described as (Zhu et al. 2021, 2023)

$$\frac{\partial N(E,t)}{\partial t} = \frac{\partial}{\partial E}[\dot{E}N(E,t)] + \frac{N(E,t)}{\tau_{\rm con}(E,t)} + \frac{N(E,t)}{\tau_{\rm diff}(E,t)} + Q(E,t), \quad (1)$$

where $N(E,t)$ is the number density of the particle, $\dot{E}$ is the total energy loss of the particle, $\tau_{\rm con}$ is the advection timescale of particle, $\tau_{\rm diff}$ is the diffusion timescale of particle, and $Q(E,t)$ is the injection term.

The total energy loss $\dot{E}$ includes synchrotron radiation loss $\dot{E}_{\rm syn}$, inverse Compton scattering loss $\dot{E}_{\rm IC}$, and the adiabatic loss $\dot{E}_{\rm ad}$. Thus, the total energy-loss $\dot{E}$ is written as

$$\dot{E} = \dot{E}_{\rm syn} + \dot{E}_{\rm IC} + \dot{E}_{\rm ad}, \quad (2)$$

where the synchrotron cooling $\dot{E}_{\rm syn}$ is given by (Rybicki & Lightman 1979)

$$\dot{E}_{\rm syn}(E_e,t) = -\frac{4}{3}\frac{\sigma_{\rm T}}{m_e c}U_{\rm B}(t)(E_e/m_e c^2)^2, \quad (3)$$

where E_e is electron energy, $\sigma_{\rm T}$ is the Thomson cross section and $U_{\rm B}(t) = B^2_{\rm pwn}(t)/8\pi$ is the energy density of the magnetic field. The inverse Compton cooling $\dot{E}_{\rm IC}$ is given by (Blumenthal & Gould 1970)

$$\dot{E}_{\rm IC}(E_e) = -\frac{3}{4}\frac{\sigma_{\rm T}h}{m_e c}\frac{1}{(E_e/m_e c^2)^2}\int_0^\infty \nu_{\rm f}d\nu_{\rm f}\int_0^\infty \frac{n(\nu_i)}{\nu_i} \times f(q,\Gamma)H(1-q)H\left(q - \frac{1}{4(E_e/m_e c^2)^2}\right)d\nu_i, \quad (4)$$

where h is the Planck constant, ν_i and ν_f are the initial and final frequencies of the scattered photons, respectively, H is the Heaviside step function, and $n(\nu_i)$ is the distribution of target photon fields. The function $f(q,\Gamma)$ can be expressed as

$$f(q,\Gamma) = 2q\ln q + (1-q)\left((1+2q) + \frac{1}{2}\frac{(\Gamma q)^2}{1+\Gamma q}\right), \quad (5)$$

with $\Gamma = 4h\nu_i(E_e/m_e c^2)/m_e c^2$ and $q = h\nu_f/\Gamma(E_e - h\nu_f)$. The adiabatic loss $\dot{E}_{\rm ad}$ is given by (Tanaka & Takahara 2010)

$$\dot{E}_{\rm ad}(E_e,t) = -\frac{V_{\rm PWN}}{R_{\rm PWN}(t)}E_e, \quad (6)$$

where $V_{\rm PWN}$ and $R_{\rm PWN}$ are the expansion velocity and the radius of the nebula, respectively.

On the other hand, the particles propagate via advection and diffusion processes. The advection velocity can be approximated as (e.g., Vorster & Moraal 2013; Zhu et al. 2021)

$$V(r) = V_{\rm PWN}(t)\left[\frac{R_{\rm PWN}(t)}{r}\right]. \quad (7)$$

The advection timescale of particles $\tau_{\rm con}$ is described as

$$\tau_{\rm con} = \int_{R_{\rm ts}(t)}^{R_{\rm PWN}(t)} \frac{1}{V(r)}dr. \quad (8)$$

where $R_{\rm ts}(t)$ is the radius of the termination shock. Combining Equations (7) and (8), $\tau_{\rm con}$ is written as

$$\tau_{\rm con} = \frac{1}{2}\tau_{\rm ad} - \frac{R_{\rm ts}(t)^2}{2V_{\rm pwn}R_{\rm pwn}(t)}. \quad (9)$$

where $\tau_{\rm ad} = E_e/\dot{E}_{\rm ad}(E_e,t)$ is the adiabatic loss timescale. The diffusion coefficient is assumed to be (e.g., Zhu et al. 2021)

$$K(t) = \frac{K(t_{\rm ini})B_{\rm pwn}(t_{\rm ini})}{B_{\rm pwn}(t)}\left[\frac{E_e}{1{\rm TeV}}\right]^\delta, \quad (10)$$

where $K(t_{\rm ini})$ and $B_{\rm pwn}(t_{\rm ini})$ are the initial diffusion coefficient and initial magnetic field strength, respectively, and $t_{\rm ini}$ is the initial birth time of the pulsar. The diffusion coefficient increases with energy, that is, $\propto E_e^\delta$. Here, the value of δ depends on the property of turbulence in the ambient medium, and the different values of δ represent different diffusion forms (for details, see Zhu et al. 2021, 2023). Following Kim et al. (2024), we assumed that the turbulence is a classical Kolmogorov turbulence within the nebula, and so the value of δ was chosen to be one-third. According to Parker (1965), the diffusion timescale of particles $\tau_{\rm diff}$ is described by

$$\tau_{\rm diff} = \frac{R^2_{\rm pwn}(t)}{6K(t)}, \quad (11)$$

A PWN is powered by the central pulsar through its spin-down. The life of a pulsar begins with an initial spin-down luminosity, and then its spin-down luminosity evolves with time, t, as (Pacini & Salvati 1973; Gaensler & Slane 2006)

$$L(t) = L_0\left(1 + \frac{t}{\tau_0}\right)^{-\frac{n+1}{n-1}}, \quad (12)$$

where L_0 is the initial luminosity, and τ_0 is the initial spin-down timescale. Most measured values for the braking index n have been found between 2 and 3 (Gaensler & Slane 2006; Ou et al. 2016), but typically $n = 3$ is assumed. This would indicate a pure magnetic dipole radiation on the pulsar's surface. The initial spin-down timescale, τ_0, is given by

$$\tau_0 = \frac{2\tau_{\rm c}}{n-1} - t, \quad (13)$$

where $\tau_{\rm c}$ is the characteristic age of the pulsar,

$$\tau_{\rm c} = \frac{P}{2\dot{P}}, \quad (14)$$

where P and $\dot{P}$ are the period and period derivative of the pulsar. In addition, the current spin-down luminosity, $L(t_{\rm age})$, can be calculated by

$$L(t_{\rm age}) = 4\pi^2 I\frac{\dot{P}}{P^3}, \quad (15)$$

where I is the moment of inertia of the pulsar, which is adopted to be 10^{45} g cm^2 in this paper. Note that the $t_{\rm age}$ is the age of the PWN. If $t = t_{\rm age}$ and n are given, the L_0 and τ_0 can be obtained.

In addition, according to the conservation of magnetic energy, the average magnetic field in the nebula $B_{\rm PWN}(t)$ is calculated with (Gelfand et al. 2009)

$$B_{\rm pwn}(t) = \left(\frac{1}{R_{\rm pwn}(t)}\right)^2 \sqrt{6\eta_{\rm B}\int_0^t L(t')R_{\rm pwn}(t')dt'}, \quad (16)$$

where $\eta_{\rm B}$ and $L(t')$ are the magnetic energy fraction and the spin-down luminosity of pulsar, respectively. In general, the spin-down luminosity $L(t)$ is assumed to be distributed between particles of energy ($\dot{E}_e(t) = \eta_{\rm e}L(t)$) and the magnetic field energy ($\dot{E}_{\rm B}(t) = \eta_{\rm B}L(t)$), where $\eta_{\rm B} + \eta_{\rm e} = 1$.

The last term on the right-hand side Equation (1), $Q(E, t)$, is typically assumed to be a broken power-law form

$$Q(E, t) = Q_0(t)\begin{cases}\left(\frac{E}{E_{\rm b}}\right)^{-\alpha_1} & \text{for } E \leqslant E_{\rm b},\\ \left(\frac{E}{E_{\rm b}}\right)^{-\alpha_2} & \text{for } E_{\rm b} \leqslant E < E_{\rm max},\end{cases} \quad (17)$$

where $Q_0(t)$ is a time-dependent normalization coefficient, $E_{\rm b}$ is the energy break, and α_1 and α_2 are low- and high-energy spectral indices, respectively. Lastly, $E_{\rm max}$ is the maximum energy of the injected electrons and positrons. The time-dependent normalization coefficient $Q_0(t)$ can be estimated by

$$(1 - \eta_B)L(t) = \int_0^{E_{\rm max}} Q(E, t)EdE, \quad (18)$$

where $L(t)$ is the spin-down luminosity of the pulsar.

Similar to Gelfand et al. (2009), the dynamical properties can be self-consistently studied for the PWN. As mentioned in Gelfand et al. (2009), the large-scale evolution of a composite supernova remnant (SNR) depends on the mechanical energy of the explosion $E_{\rm sn}$, the density of the ambient medium $\rho_{\rm ISM}$, the mass of the supernova ejecta $M_{\rm ej}$, and the spin-down power of the pulsar $L(t)$. The evolution of the SNR radius $R_{\rm SNR}(t)$, the reverse shock radius $R_{\rm rs}(t)$, the PWN radius $R_{\rm PWN}(t)$, and the termination shock radius $R_{\rm ts}(t)$ of the system can be calculated. The calculation process here is the same as in Gelfand et al. (2009; for details, see their Section 2.2).

3. Result

As mentioned in Section 1, the central pulsar J1849-0001 has a spin period of $P = 38.52$ ms and a period derivative of $\dot{P} = 14.14 \times 10^{-15}$ s s^{-1}. Nowadays, this pulsar has the 16th highest $L(t_{\rm age})$ out of the 2400 pulsars known in our Galaxy (Manchester et al. 2005), and Suzuki et al. (2021) considered the discrepancies of the characteristic ages of the associated pulsars with the true age are sometimes larger. Consequently, it must be relatively young. Following Kim et al. (2024), the age of the system is estimated as $t_{\rm age} = 9000$ yr. For the measured P and $\dot{P}$ values of the pulsar, the corresponding characteristic age is $\tau_c = 4.31 \times 10^4$ yr and the current spin-down luminosity is $L(t_{\rm age}) = 9.77 \times 10^{36}$ erg s^{-1}. With Equations (12) and (13), the initial spin-down timescale $\tau_0 = 3.41 \times 10^4$ yr and the initial luminosity $L_0 = 1.56 \times 10^{37}$ erg s^{-1} are estimated. Lastly, Terrier et al. (2008) used the hydrogen column density to estimate the distance of the pulsar, about 7 kpc, which is adopted here.

As for the observed multiband data, the X-ray data are taken from Gagnon et al. (2023), Fermi-LAT upper limits are taken from Eagle (2022), TeV data are taken from H.E.S.S. Collaboration (2018b) and Amenomori et al. (2023), and PeV data are taken from Cao et al. (2024). Furthermore, the X-ray images have revealed the angular radius $\theta_{\rm X-ray} \sim 150''$ (Gotthelf et al. 2011; Gagnon et al. 2023; Kim et al. 2024) and the corresponding radius $R_{\rm X-ray} \sim 5.0$ pc for the distance of 7.0 kpc. In addition, H.E.S.S. observations show the angular radius $\theta_\gamma \sim 0.^\circ09$ and the corresponding radius $R_\gamma \sim 11.0$ pc. For the radio upper limit, following Gagnon et al. (2023), a 2σ GLOSTAR survey limit at 6.9 GHz is given.

To calculate the spectral energy distributions (SED) of observed multiband nonthermal photons, the particle spectrum at the current time ($N(E, t)$) is obtained by solving the transport equation of particles (Equation (1), here $t = t_{\rm age} = 9000$ yr), and then the SEDs of nonthermal photons are calculated through synchrotron radiation and IC scattering of relativistic electrons and positrons within the PWN. In our calculation, the target photons consist of three components: the cosmic microwave background (CMB) photons, the galactic near-infrared (NIR) photons, and far-infrared (FIR) photons. The energy densities $U_{\rm CMB} = 0.25$ eV cm^{-3}, $U_{\rm IR} = 1.25$ eV cm^{-3}, and $U_{\rm NIR} = 1.26$ eV cm^{-3}, and temperatures $T_{\rm CMB} = 2.7$ K, $T_{\rm IR} = 20$ K and $T_{\rm NIR} = 3000$ K for the CMB, and NIR and FIR photons are used in the calculation. The energy densities of the fields are obtained based on the radiation transfer model for the Milky Way (Popescu et al. 2017).

As shown in Figure 1, the left panel represents the electron spectrum of the nebula, and the right panel shows that the multiband data are reproduced well by synchrotron and IC emission of relativistic electrons and positrons, and the related parameters are listed in Table 1. In the process, the SN parameters are fixed. These parameter values are generally measured or assumed, and the spectral parameters, $E_{\rm b}$, α_1 and α_2, the magnetic fraction, $\eta_{\rm B}$, the maximum energy of particles, $E_{\rm max}$, and the initial diffusion coefficient, $K(t_{\rm ini})$ as fitted parameters. Here, the Levenberg–Marquardt (LM) method of the χ^2 minimization fitting procedure (Press et al. 1992) is used to obtain the best-fitting values for the fitting process. In addition, the derived parameters (PWN magnetic field $B_{\rm pwn}$ and radius $R_{\rm pwn}$) are also represented in Table 1.

Our model indicates a low magnetic field strength of $\sim 2.8\ \mu G$, which is consistent with the value estimated by Kim et al. (2024) using similar fluxes of X-ray and TeV. In addition, Gagnon et al. (2023) used a model that does not include the cooling and transport processes to reproduce well the observed multiband data, inferring a value of the magnetic field, 1–2 μG. Meanwhile, the presented model here gives $R \sim 11.0$ pc, which is consistent with the PWN-measured size in the TeV band (H.E.S.S. Collaboration 2018b). Note that the radius $R \sim 5$ pc is obtained in the theoretical model of Gagnon et al. (2023) and Kim et al. (2024), consistent with the X-ray size.

From the modeling results, the low-energy spectral index has a value of $\alpha_1 \sim 1.45$, the high-energy index is $\alpha_2 \sim 2.54$, the energy break is $E_{\rm b} \sim 5.97 \times 10^5$ MeV, the magnetic fraction is $\eta_{\rm B} \sim 0.033$, and the initial diffusion coefficient is $K(t_{\rm ini} \sim 0) \sim 3.22 \times 10^{22}$ cm^2 s^{-1}. These fitting results are similar to those values previously obtained in typical PWNe (Torres et al. 2014; Zhu et al. 2018, 2023). Quite importantly, particles injected in

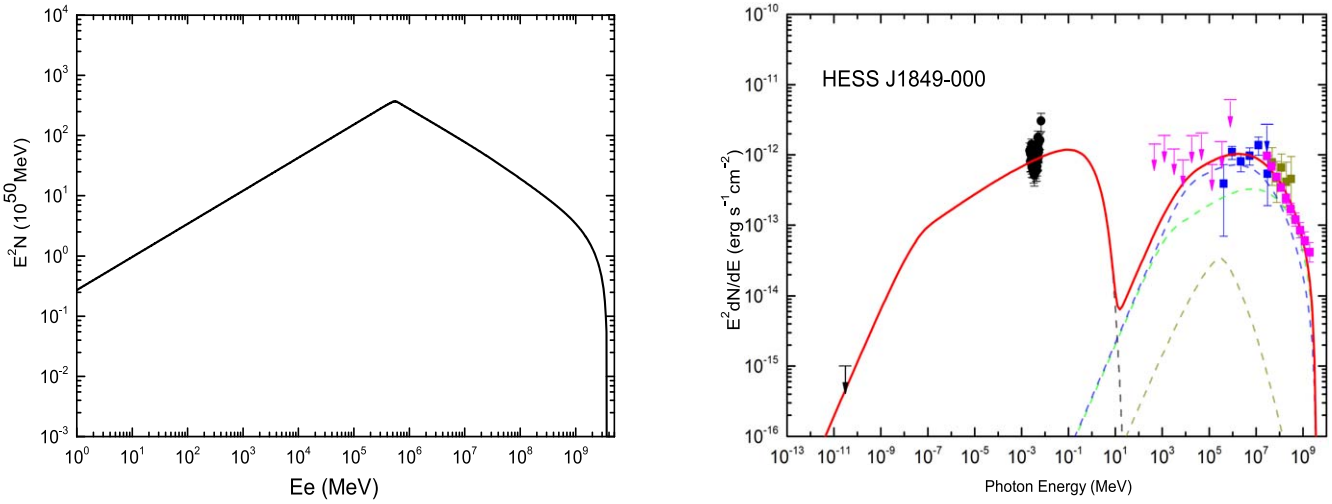

Figure 1. The left panel shows the electron spectra at current time $t_{age} = 9000$ yr. The right panel shows a comparison of calculated multiband SED with the observed data for HESS J1849-000; the black dashed line represents synchrotron SED; the blue, green, and dark yellow dashed lines represent the SEDs of inverse Compton scatterings with the IR, CMB, and starlight, respectively. The black upper limit represents the GLOSTAR survey limit (Brunthaler et al. 2021), the black points display X-ray measurements (Gagnon et al. 2023), the magenta upper limits represent the Fermi-LAT measurements (Eagle 2022), the blue squares correspond to H.E.S.S. measurements (H.E.S.S. Collaboration 2018a), the dark yellow squares represent Tibet ASγ measurements (Amenomori et al. 2023), and the magenta squares display LHAASO measurements (Cao et al. 2024).

Table 1
Values of Physical Parameters Used for HESS J1849-000

Pulsar and Ejecta Parameters	Symbol	Value
Period (ms)	P	38.52
Period derivative (ss^{-1})	$\dot{P}$	1.41×10^{-16}
Braking index	n	3.0
Distance (kpc)	d	7.0
Characteristic age	τ_c	4.31×10^4
Spin-down luminosity (ergs $^{-1}$)	$L(t_{age})$	9.77×10^{36}
Initial spin-down power (ergs $^{-1}$)	L_0	1.56×10^{37}
Initial spin-down timescale (yr)	τ_0	3.41×10^4
Age (yr)	t_{age}	9000
SN explosion energy (10^{51} erg)	E_{SN}	1.5
Ejected mass ($M_\odot$)	M_{ej}	6.0
ISM density (cm^{-3})	n_H	0.01
Fitted Parameters		
Magnetic fraction	η_B	0.033
Low-energy electron index	α_1	1.45
High-energy electron index	α_2	2.54
Break energy (10^5 MeV)	E_b	5.97
Maximum energy (PeV)	E_{max}	3.65
Initial diffusion coefficient ($10^{22}cm^2s^{-1}$)	K(t_{ini})	3.22
Resulting Features		
PWN magnetic field (μ G)	B_{PWN}	2.76
PWN radius (pc)	R_{PWN}	10.89
Reduced χ^2	1.13	...

the PWNe can be accelerated up to ~3.6 PeV, which makes HESS J1849-000 a PeVatron candidate.

To understand the transport and cooling mechanisms for the particles within HESS J1849-000, the timescales considered are shown in the left panel of Figure 2. The effect of relevant physical processes increases with the decrease of the corresponding timescale since the shorter timescales result in a more effective cooling effect. The particle cooling process includes the adiabatic loss, synchrotron radiation loss, and IC scattering losses. Thus, the corresponding particle cooling timescale $\tau(E_e, t) = E_e/\dot{E}_e(E_e, t)$ is the sum of the synchrotron radiation loss timescale $\tau_{syn} = E_e/\dot{E}_{syn}(E_e, t)$, the inverse Compton scattering loss timescale $\tau_{ic} = E_e/\dot{E}_{ic}(E_e)$, and the adiabatic loss timescale $\tau_{ad} = E_e/\dot{E}_{ad}(E_e, t)$. The effects of the cooling mechanisms are dominated by adiabatic loss for $E_e < 5.0 \times 10^7$ MeV bands, the IC scattering losses dominate over the synchrotron loss and adiabatic loss for 5.0×10^7 MeV $< E_e < 4.5 \times 10^8$ MeV bands, and synchrotron loss dominates over the adiabatic loss and IC scattering losses for $E_e > 4.5 \times 10^8$ MeV band. On the other hand, the particle transport process includes advection and diffusion. The advection is the most prominent process for $E_e < 1.1 \times 10^8$ MeV bands, and the effect of diffusion increases with the increase of energy. Lastly, the diffusion becomes the dominant process for $E_e > 1.1 \times 10^8$ MeV. We also obtain the current diffusion coefficient $\sim 3.4 \times 10^{26}$ cm^2 s^{-1} at the electron energy of 1 TeV by the model. Lastly, the total timescale, $\tau_{eff} = (1/\tau_{ad} + 1/\tau_{syn} + 1/\tau_{ic} + 1/\tau_{diff} + 1/\tau_{con})^{-1}$, is also shown in Figure 2.

To compare the dominance between the transport and energy losses, following Lu et al. (2023), the total energy cooling timescale is given by

$$\tau_C = \left[\frac{1}{\tau_{ad}} + \frac{1}{\tau_{syn}} + \frac{1}{\tau_{ic}}\right]^{-1}, \quad (19)$$

and the total transport timescale is written by

$$\tau_P = \left[\frac{1}{\tau_{diff}} + \frac{1}{\tau_{con}}\right]^{-1}. \quad (20)$$

When $\tau_P/\tau_C < 1.0$, the importance of particle transport processes dominate over that of the cooling process. On the contrary, when $\tau_P/\tau_C > 1.0$, the importance of particle cooling processes dominates over that of the transport process. The ratio of the total particle transport timescale to the total cooling timescale is shown in the right panel of Figure 2. Our results show that the particle transport would play a significant role for

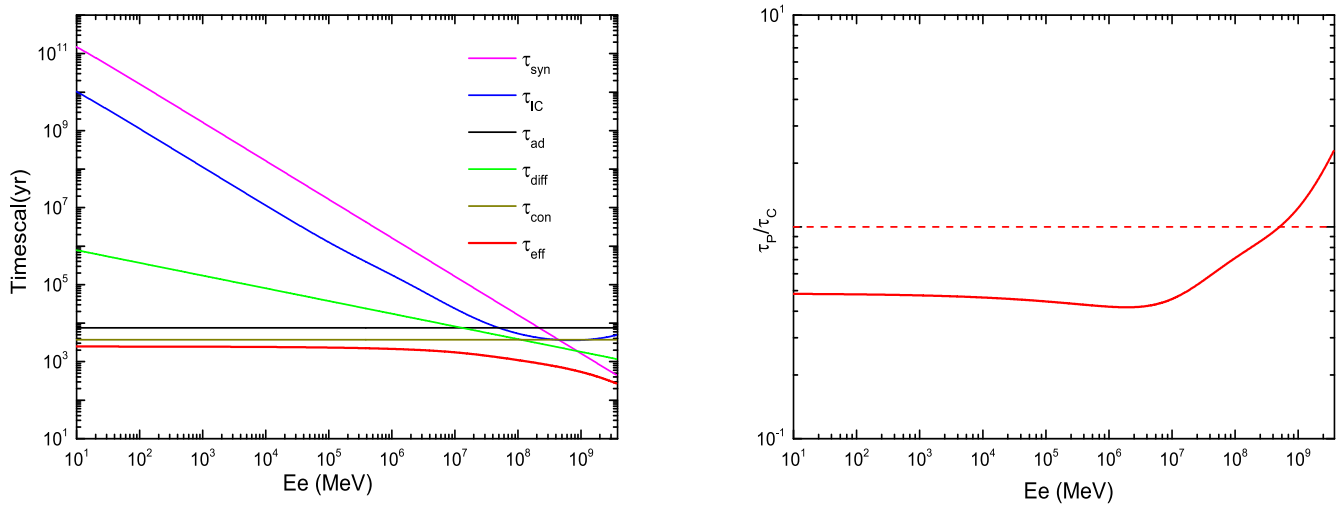

Figure 2. The left panel: the different timescales at the current time. The solid back, magenta, blue, green, dark yellow, and red lines represent the adiabatic loss timescale, the synchrotron cooling timescale, the inverse Compton cooling timescale, the diffusion timescale, the advection timescale, and the total timescale, respectively. The right panel: the red line represents the timescale ratio of the particle transport to cooling, and the red dashed line represents the corresponding ratio = 1.0.

the $E_e < 5.0 \times 10^8$ MeV, while the particle cooling process plays a more important role than the transport process for $E_e > 5.0 \times 10^8$ MeV.

4. Conclusion and Discussions

In this paper, we applied the spectral evolution model involving the particle transport and cooling processes to study the multiband nonthermal radiative properties of HESS J1849-000. In this model, it is assumed that the electrons and positrons injected into the nebula have a power-law-breaking distribution. As exhibited in the right panel of Figure 1, considering the synchrotron radiation and inverse Compton process of the relativistic leptons, the observed spectral energy distributions in X-ray and γ-ray bands are reproduced well.

Our model predicts the magnetic field strength $B_{\rm PWN} \sim 3\mu G$, which is consistent with results obtained in typical PWNe (Torres et al. 2014; Zhu et al. 2018). Moreover, a low magnetic field was found for other PeVatron candidates PWNe (Joshi et al. 2022). Additionally, the radius of nebula $\sim$11.0 pc is consistent with the TeV observation results (H.E.S.S. Collaboration 2018b).

In addition, our studies suggest that HESS J1849-000 can be a PeVatron candidate as there are particles that can be accelerated up to 3.6 PeV. Generally, several radiation fields supply target photons for the IC scattering of electrons within nebulae. However, at energies above 100 TeV, the CMB radiation dominates the γ-ray photon production (for details, see Figures 1–3 of Zhu et al. 2018). Thus, above 100 TeV energies of the upscattered photon E_γ and the parent electron E_e are linked through the simple relation $E_e \simeq 2.15(E_\gamma/1\ {\rm PeV})^{0.77}$ (Cao et al. 2021b). Amenomori et al. (2023) measured the spectrum of HESS J1849-000 at TeV energies and found no evidence of cut-off up to 740 TeV, which implies the corresponding electron energy of $E_e \simeq 1.7$ PeV. Furthermore, the LHAASO observation detects γ-ray photons up to 1.9 PeV (Cao et al. 2024), and it implies the corresponding electron energy of $E_e \simeq 3.5$ PeV. The result is consistent with these theoretical values. In fact, HESS J1849-000 reveals common features to previous PWNe with maximum particle energies above 1 PeV, e.g., Crab Nebula (Cao et al. 2021b), Eel (Burgess et al. 2022), Dragonfly (Woo et al. 2023) and Boomerang (Pope et al. 2024).

Lastly, as shown in Figure 2, our model shows the adiabatic loss dominates over the synchrotron and inverse Compton losses in the low-energy band, and the synchrotron loss dominates over adiabatic loss and inverse Compton losses in the high-energy band. Whereas, the advection dominates over the diffusion process in the low-energy band, and the diffusion plays a prominent role in the high-energy band. On the other hand, our result also indicated that particle transport dominates over cooling losses for the low-energy bands and particle cooling losses dominate over transport for the high-energy band. In fact, these results are consistent with previous studies for typical PWNe (Lu et al. 2020; Zhu et al. 2021, 2023). We found that the current diffusion coefficient $\sim 3.4 \times 10^{26}\ {\rm cm^2\ s^{-1}}$ at the electron energy of 1 TeV. It is about 3 orders of magnitude smaller than the average value obtained by fits to the AMS-02 boron-to-carbon ratio data in the Galaxy (Kappl et al. 2015; Genolini et al. 2019). The result is consistent with previous studies, i.e., the slow-diffusion mechanism may exist within a certain group of PWNe (Di Mauro et al. 2020; Zhu et al. 2021, 2023).

Acknowledgments

We would like to thank the anonymous referee for the very valuable comments. L.Z. is partially supported by the National Natural Science Foundation of China (NSFC) under grant 12233006. B.T.Z. is partially supported by NSFC under grant 12363007, Yunnan Fundamental Research Projects Province (No. 202101AU070099, 202301AS070073), and Xingdian Talent Support Program of Yunnan Province. F.W.L. is partially supported by NSFC under grant 12363006, Yunnan Fundamental Research Projects (No. 202201AT070234), Xingdian Talent Support Program of Yunnan Province, and the Program for Innovative Research Team (in Science and Technology) in the University of Yunnan Province (IRTSTYN).

ORCID iDs

Li Zhang https://orcid.org/0000-0002-7824-4289

References

Amenomori, M., Asano, S., Bao, Y. W., et al. 2023, ApJ, 954, 200
Anderson, L. D., Wang, Y., Bihr, S., et al. 2017, A&A, 605, A58
Blumenthal, G. R., & Gould, R. J. 1970, RvMP, 42, 237
Brunthaler, A., Menten, K. M., Dzib, S. A., et al. 2021, A&A, 651, A85
Burgess, D. A., Mori, K., Gelfand, J. D., et al. 2022, ApJ, 930, 148
Cao, Z., Aharonian, F., An, Q., et al. 2021a, Natur, 594, 33
Cao, Z., Aharonian, F., An, Q., et al. 2021b, Sci, 373, 425
Cao, Z., Aharonian, F., An, Q., et al. 2024, ApJS, 271, 25
Di Mauro, M., Manconi, S., & Donato, F. 2020, PhRvD, 101, 103035
Eagle, J. 2022, arXiv:2209.11855
Gaensler, B. M., & Slane, P. O. 2006, ARA&A, 44, 17
Gagnon, S., Kargaltsev, O., Klingler, N., et al. arXiv:2311.13677
Gelfand, J. D., Slane, P. O., & Zhang, W. 2009, ApJ, 703, 2051
Genolini, Y., Boudaud, M., Batista, P. I., et al. 2019, PhRvD, 99, 123028
Gotthelf, E. V., Halpern, J. P., Terrier, R., & Mattana, F. 2011, ApJL, 729, L16
Green, D. A. 2014, BASI, 42, 47
Green, D. A. 2019, JApA, 40, 36
H.E.S.S. Collaboration 2018a, A&A, 612, A2
H.E.S.S. Collaboration 2018b, A&A, 612, A1
Joshi, J. C., Tanaka, S. J., Miranda, L. S., & Razzaque, S. 2022, MNRAS, 520, 5858
Kappl, R., Reinert, A., & Winkler, M. W. 2015, JCAP, 10, 034
Kim, S., Park, J., Woo, J., et al. 2024, ApJ, 960, 78
Kuiper, L., & Hermsen, W. 2015, MNRAS, 449, 3827
Lu, F.-W., Gao, Q.-G., & Zhang, L. 2020, MNRAS, 498, 1911
Lu, F.-W., Zhu, B.-T., Hu, W., & Zhang, L. 2023, MNRAS, 518, 3949
Manchester, R. N., Hobbs, G. B., Teoh, A., & Hobbs, M. 2005, AJ, 129, 1993
Molkov, S. V., Cherepashchuk, A. M., Lutovinov, A. A., et al. 2004, AstL, 30, 534
Ou, Z. W., Tong, H., Kou, F. F., & Ding, G. Q. 2016, MNRAS, 457, 3922
Pacini, F., & Salvati, M. 1973, ApJ, 186, 249
Parker, E. N. 1965, P&SS, 13, 9
Pope, I., Mori, K., Abdelmaguid, M., et al. 2024, ApJ, 960, 75
Popescu, C. C., Yang, R., Tuffs, R. J., et al. 2017, MNRAS, 470, 2539
Press, W. H., Teukolsky, S. A., Vetterling, W. T., & Flannery, B. P. 1992, Numerical Recipes in C. The Art of Scientific Computing (Cambridge: Cambridge Univ. Press)
Rybicki, G. B., & Lightman, A. P. 1979, Radiative Processes in Astrophysics (New York: Wiley)
Suzuki, H., Bamba, A., & Shibata, S. 2021, ApJ, 914, 103
Tanaka, S. J., & Takahara, F. 2010, ApJ, 715, 1248
Terrier, R., Mattana, F., Djannati-Atai, A., et al. 2008, in AIP Conf. Ser. 1085, Proc. 4th Int. Meeting on High Energy Gamma-Ray Astronomy (Melville, NY: AIP), 312
Torres, D. F., Cillis, A., Martín, J., & de Oña Wilhelmi, E. 2014, JHEAp, 1, 31
Vleeschower Calas, L., Kaufmann, S., Alvarez Ochoa, C., & Tibolla, O. 2018, NPPP, 297-299, 102
Vorster, M. J., & Moraal, H. 2013, ApJ, 765, 30
Woo, J., An, H., Gelfand, J. D., et al. 2023, ApJ, 954, 9
Zhu, B. T., Lu, F. W., & Zhang, L. 2023, ApJ, 943, 89
Zhu, B. T., Lu, F. W., Zhou, B., & Zhang, L. 2021, A&A, 655, A41
Zhu, B. T., Zhang, L., & Fang, J. 2018, A&A, 609, A110